frontiers | Frontiers in Chemistry

TYPE Original Research
PUBLISHED 09 January 2023
DOI 10.3389/fchem.2022.1102528

OPEN ACCESS

EDITED BY
Chao Liu,
Yancheng Institute of Technology, China

REVIEWED BY
Zhongjie Guan,
Henan University, China
Shijie Li,
Zhejiang Ocean University, China

*CORRESPONDENCE
Xiaoge Wu,
xgwu@yzu.edu.cn
Weihua Peng,
pengweihuapwh@126.com
Jianhua Hou,
jhhou@yzu.edu.cn

SPECIALTY SECTION
This article was submitted to Catalytic Reactions and Chemistry, a section of the journal Frontiers in Chemistry

RECEIVED 19 November 2022
ACCEPTED 05 December 2022
PUBLISHED 09 January 2023

CITATION
Wu X, Qin N, Yan L, Ji R, Wu D, Hou Z, Peng W and Hou J (2023), *In situ* preparation of a $Bi_2O_2CO_3$/BiOI with 2D/2D p-n heterojunction photocatalyst for water purification under visible light.
Front. Chem. 10:1102528.
doi: 10.3389/fchem.2022.1102528

In situ preparation of a $Bi_2O_2CO_3$/BiOI with 2D/2D p-n heterojunction photocatalyst for water purification under visible light

Xiaoge Wu[1]*, Nan Qin[1], Lei Yan[1], Renlong Ji[2], Di Wu[3], Zhenhua Hou[3], Weihua Peng[4]* and Jianhua Hou[1]*

[1]College of Environmental Science and Engineering, Yangzhou University, Yangzhou, Jiangsu, , China, [2]College of Materials Science and Engineering, Yantai Nanshan University, Longkou, Shandong, China, [3]Jiangxi Xinda Hangke New Materials Technology Co., Ltd., Nanchang, China, [4]Key Laboratory of Mine Water Resource Utilization of Anhui Higher Education Institutes, Suzhou University, Suzhou, China

Introduction: Semiconductors have similar crystal structures and matched energy levels could form a coupled heterojunction at an interface between them which may allow response to visible light, achieving efficient decomposition of organic compounds.

Methods: The $Bi_2O_2CO_3$/BiOI (BOC/BOI) with 2D/2D p-n heterojunction was prepared by one-pot room-temperature strategy. The prepared materials were tested by various technologies, and the three-dimensional structure, light absorption properties, electrochemical properties and other information were obtained. Photocatalytic tests have also been carried out.

Results and discussion: BOC/BOI heterojunction with oxygen vacancies showed much higher photocatalytic activity than pure BOC and BOI. For example, the preferred BOC/BOI-0.5 heterojunction of the degradation rate for Rhodamine B (RhB) is 97.6 % within 2 h, which is 15.8 and 2.2 times faster than that of BiOI and BOC. In addition, the removal rates of tetracycline, ciprofloxacin and bisphenol A by BOC/ BOI-0.5 were 92.4, 80.3 and 68.6%, respectively. The 2D/2D structures of BOC/BOI-0.5 with rich in oxygen vacancies combined p-n junction can effectively inhibit the photoinduced electron-hole pair recombination and increase the production of active free radicals. The O_2- and h+ are the main reactants, giving the composite catalyst potential for degrading a variety of pollutants.

KEYWORDS

$Bi_2O_2CO_3$, BiOI, p-n heterojunctions, photocatalysis, water purification

1 Introduction

Rapid industrialization and increasing environmental problems have made organic pollutants a prominent and difficult problem worldwide (Feng et al., 2018; Liu et al., 2018). Photocatalysts have much to offer in dealing with such energy and environmental problems, but the photocatalytic activity of many photocatalysts is by their response range and quantum efficiency (Sakthivel et al., 2020; Xu et al., 2020). It has been reported (Hamza et al., 2020) that the heterostructured photocatalysts such as $Bi_2O_2CO_3/Bi_2WO_6$ (Qiang et al., 2021), g-C_3N_4/BiOI (Hou et al., 2021a), $BiVO_4/Ag_3VO_4$ (Liu et al., 2021b) and BiOCl/Bi2O2CO3 (Hou et al., 2020b) can combine the advantages of two or more semiconductor materials with matching band structures with good light absorption and charge separation.

The 2p valence band of oxygen and bismuth's 6s valence band make bismuth-containing semiconductors stand out from other heterostructured photocatalysts (Li et al., 2018; Zhang et al., 2020). Bismuth oxyiodide (BiOI) and bismuth carbonate oxide ($Bi_2O_2CO_3$) with have a Sillén-structure in which the Bismuth, oxygen, iodine or carbonate are orthogonal to each other (Xu et al., 2017), Alternating growth in its crystal structure easily forms layered structures. Different rates of crystal growth facilitate the synthesis of 2D structures which expose specific crystal planes, or 3D structures assembled from 2D structural elements (Chen et al., 2018). A two-dimensional structure, or a three-dimensional structure consisting of two-dimensional sheets exhibits strong photocatalytic activity due to the high surface energy and large specific surface area of such structures (Shi et al., 2018). In addition, the internal electric field formed between the interlaminations can promote the effective separation of photogenerated electrons and holes, which also improves the photocatalytic performance (Di et al., 2017). However, $Bi_2O_2CO_3$'s wide band gap (2.87–3.58eV) can only be activated under UV irradiation (Zu et al., 2021), and the narrow band gap of BiOI (1.73–1.92eV) also greatly limits its further development in the degradation of organic pollutants (Lu et al., 2021). Considering that BiOI and $Bi_2O_2CO_3$ have similar crystal structures and matched energy levels, a coupled heterojunction can be formed at an interface between them which may allow response to visible light, improving the effective separation of light-induced electron-hole pairs, improving the adsorption dyestuffs (Qi et al., 2022), and achieving efficient decomposition of organic compounds (Chen et al., 2022).

This study therefore aimed to synthesize $Bi_2O_2CO_3$/BiOI heterojunction photocatalysts with enhanced photo-responsive activity applying one-pot synthesis at room temperature. The photocatalytic activity of the $Bi_2O_2CO_3$/BiOI heterojunctions synthesized was tested in Rhodamine B (RhB) degradation. Changing the molar ratio of the reactants altered the photocatalytic performance as expected. And the $Bi_2O_2CO_3$/BiOI heterojunction catalyst displayed very high photocatalytic activity into RhB degradation under visible light.

2 Experiments

2.1 Materials preparation

The chemicals used in the catalysts' preparation—potassium iodide (KI), bismuth nitrate ($Bi(NO_3)_3{\cdot}5H_2O$), urea (CH_4N_2O), nitric acid (HNO_3) and the scavenging agents ethylenediaminetetraacetic acid disodium salt (EDTA-2Na), isopropyl alcohol and benzoic acid—as well as the Rhodamine B were purchased from Sinopharm Chemical Reagent Co., Ltd. (China). All of the chemicals were of analytical grade.

$Bi_2O_2CO_3$ was obtained by mixing 970.2 mg of $Bi(NO_3)_3{\cdot}5H_2O$ with 12 ml of nitric acid, and then adding 200 ml of pure water. The mixture was stirred at 25°C for 0.5 h, and the pH was adjusted to 10 using ammonia solution. 106 mg of Na_2CO_3 was then added and stirred for 12 h. The supernatant was removed, centrifuged and washed three times, and the BOC mixture was dried at 60°C.

A similar procedure was involved in the preparation of the BiOI. 970.2 mg of $Bi(NO_3)_3{\cdot}5H_2O$ was mixed with 12 ml of nitric acid, and then 200 ml of pure water was added. The mixture was stirred at 25°C for 0.5 h, the pH was adjusted to 10 using ammonia solution. 622 mg of KI was then added and stirred at 25°C for 12 h. The supernatant was removed, centrifuged and washed three times, and the resulting BOI mixture was dried at 60°C.

The binary catalyst was synthesized by dissolving 970.2 mg of $Bi(NO_3)_3{\cdot}5H_2O$ in 12 ml of nitric acid, adding 200 ml of pure water, and stirring at 25°C for 0.5 h. After adjusting the pH to 10 with ammonia, 106 mg of Na_2CO_3 was added and the suspension was stirred for 0.5 h. Either 83 mg, 166 mg, 322 mg, 622 mg or 1,244 mg of KI was added, and then sufficient $Bi(NO_3)_3{\cdot}5H_2O$ was added to make the molar ratio with KI 4:1, 2:1, 1:1, 1:2 or 1:4. The mixture was stirred at 25°C for 12 h, and the supernatant was removed, centrifuged, washed three times, and dried at 60°C. The $Bi_2O_2CO_3$/BiOI heterojunction catalysts obtained were designated BOC/BOI-4, BOC/BOI-2, BOC/BOI-1, BOC/BOI-0.5 BOC/BOI-0.25 to reflect the molar ratios.

2.2 Characterization

X-ray diffraction (XRD) analysis was recorded using a Bruker D8 Advance X-ray diffractometer with Cu K_α radiation (λ = 1.5406Å) as the X-ray source. Fourier transform infrared spectroscopy (FT-IR) was performed using a TENSOR27 spectrometer. The surface elements were detected using an ESCALAB 250Xi X-ray photoelectron spectroscope (Thermo Fisher Scientific). An A300-10/12 Bruker EPR spectrometer was used to measure the electron paramagnetic resonance (EPR) of the free radicals detected. The morphology and microstructure of the catalyst were examined using a Hitachi,

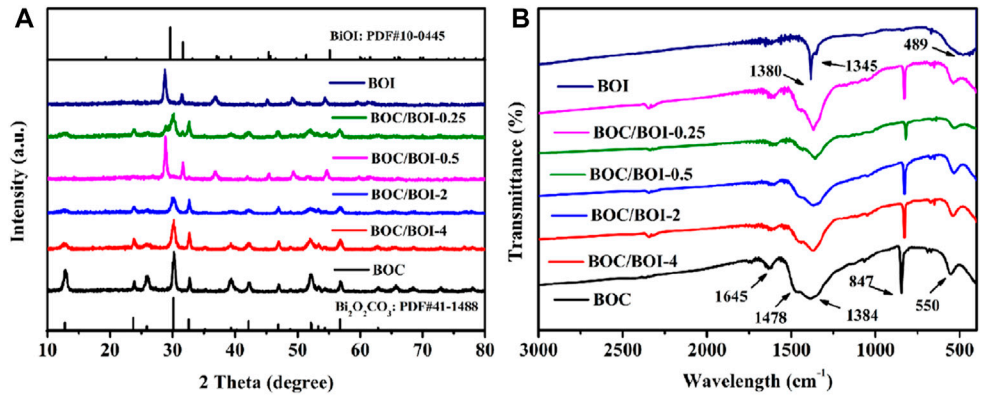

FIGURE 1
(A) XRD patterns, **(B)** FT-IR spectra of all samples.

S-4800 scanning electron microscope and high-resolution transmission electron microscopy (HRTEM) was performed with a Tecnai G2 F30 S-Twin instrument. The catalysts' optical properties were characterized by UV-visual diffuse reflectance spectroscopy relying on a Hitachi U-4100 instrument. A Micromeritics ASAP 2460 instrument was used to record the Brunauer Immett Teller (BET) specific surface areas. A Renishaw inVia confocal Raman microscope was used to study the catalysts' photoluminescence (PL). Electrochemical impedance spectroscopy (EIS) was performed and Mott Schottky diagrams were prepared in 0.2 M Na_2SO_4 electrolyte using a CHI760E electrochemical workstation. The ITO glass electrode was loaded with a sample containing 10 mg of a catalyst, and Ag/AgCl and Pt wires were used to form a three-electrode system. The EIS was over a frequency range of 0.01–10^5 Hz at 5 mV AC. The frequency of the Mott Schottky test was fixed at 10 Hz. Absorbance readings at 554 nm using a Shimadzu UV-2450 ultraviolet-visible spectrophotometer measured the concentration of RhB.

2.3 Photocatalysis tests

For RhB removal, 20 mg of catalyst was mixed with 50 ml of a 20 mg L^{-1} solution of RhB, and the suspension was stirred continuously in the dark for 1 h. The mixture was then illuminated with a 300 W xenon lamp (λ > 420 nm), and the 3 ml of the reaction mixture was sampled every 20 min to determine the RhB concentration using the UV-visible spectrophotometer.

In other experiments, 30 mg of the catalyst was mixed with 50 ml of a 10 mg L^{-1} solution of bisphenol A (BPA) and same procedure was followed. Ciprofloxacin (CIP) and tetracycline (TC) degradation were also tested in the same way (Li et al., 2022a).

3 Results and discussion

3.1 Characterization

The prepared samples were characterized using XRD with the results exhibited in Figure 1A. The pure BOC and pure BiOI peaks match the standard cards (JCPDS No. 41-1488 [Qiang et al., 2021) and JCPDS445 (Wang et al., 2017)]. Moreover, the BOC/BOI composite exhibits the coexistence of BOC and BOI phases. The diffraction peak intensity of BOI increases continuously with the KI concentration, while that of $Bi_2O_2CO_3$ decreases in tandem, indicating that BOC gradually transforms into BOI. The diffraction peak of BOC is barely detectable in the BOC/BOI-0.25 material, indicating that most of the BOC had become BOI.

Infrared spectroscopy was used to explore the chemical composition and chemical bonding of the composites (Li et al., 2022b). Figure 1B presents the FT-IR results. The strong absorption is mainly concentrated in the 400–1750 cm^{-1} region. The bands around 550 and 846 cm^{-1} arise from stretching vibration of Bi-O bonds in BOC, and those around 1,384 and 1478 cm^{-1} are attributable to the stretching vibration of C-O and C=O. The peak at 1,645 cm^{-1} relates to the out-of-plane bending vibration of CO_3^{2-} (Zu et al., 2021), The peaks of BOI at 1,380 and 1345 cm^{-1} are attributable to the -OH bending vibration of adsorbed H_2O molecules on the BOI. There is only one peak at about 489 cm^{-1} due to the stretching vibration of Bi-O bonds in BOI (Hou et al., 2021a).

BOC characteristic bands persist in the BOC/BOI composite. As the composite's BOI content increases, Bi-O bond traces at 550 cm^{-1} gradually move to lower frequencies (compare BOC/BOI-4 to BOC/BOI-0.25). The peak intensities of C-O and C=O at 1384 and 1,478 cm^{-1} also gradually decrease, which proves that BOC and BOI coexist in the composite. No absorption peaks attributable to impurities or solvent residue were detected.

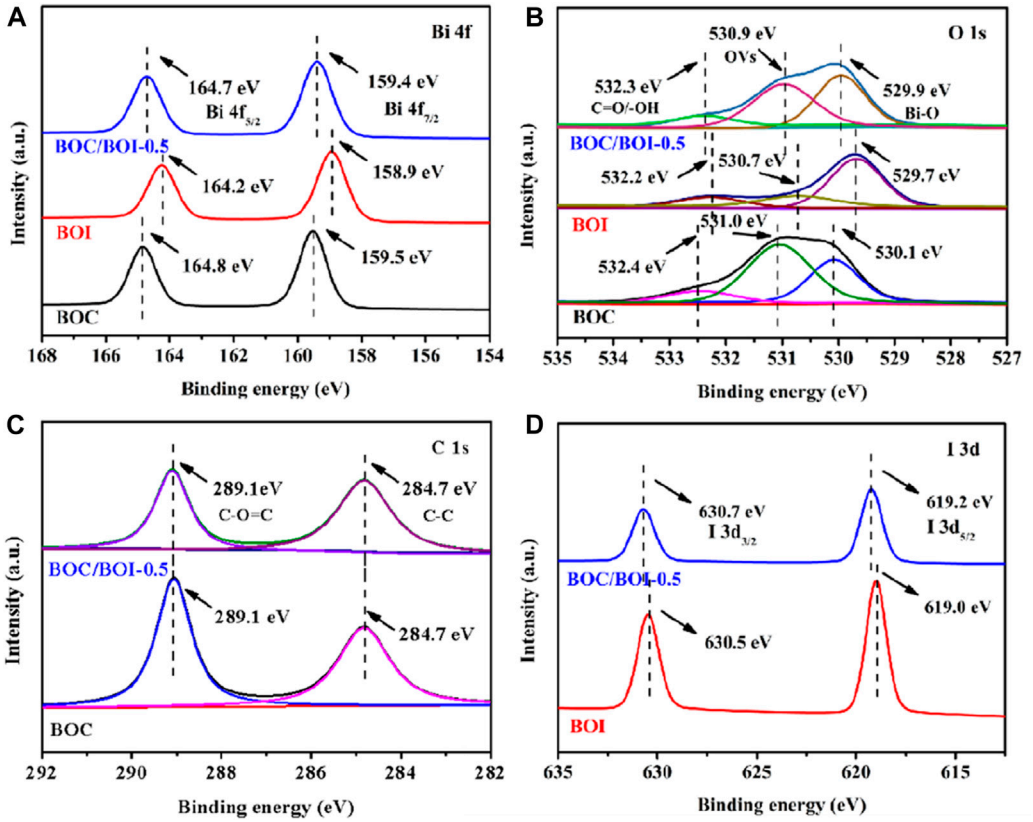

FIGURE 2
XPS spectra of the **(A)** Bi 4f, **(B)**O 1s, **(C)** C 1s and **(D)** I 3d orbitals of BOC, BOI and BOC/BOI-0.5.

The XPS spectra show the surface chemical states of the photocatalytic materials. The full spectrum survey revealed only Bi, O, C, and N in the BOC. The small amount of N may indicate the presence of $BiONO_3$. The excess C content is due to the adsorption of carbon from the air. The curves for BOC/BOI-0.5 in Supplementary Figure S1 indicate the presence of Bi, O, C, and I simultaneously, indicating that BOC and BOI effectively coexist.

In Figure 2A BOC (159.5 and 164.8 eV) and BOI (158.9 and 164.2 eV) have doublet peaks (attributable to Bi $4f_{7/2}$ and Bi $4f_{5/2}$). For BOC/BOI-0.5, the peaks attributable to Bi 4f can be decomposed into 159.4 and 164.7 eV, corresponding to the characteristics of Bi^{3+} (Tang et al., 2020). In Figure 2B, the X-ray photoelectron spectrum, of oxygen's 1s orbital in BOC/BOI-0.5 can be ascribed to the peak at 529.9 eV due to the Bi-O bond in $[Bi_2O_2]^{2+}$ (Ding et al., 2019). The other two characteristic peaks, the possible corresponding oxygen vacancy at 530.9 eV, and the binding energy peak at 532.3 eV, are due to the C=O bond of BOC (532.3 eV) and the surface hydroxyl group of BOI (532.2 eV) (Zhao et al., 2019a). The binding energies of BOC/BoI-0.5 in terms of both the Bi 4f and O 1s orbitals are between those of BOC and BOI. This indicates that $Bi_2O_2CO_3$/BiOI may have a heterojunction (Li et al., 2022c). For the carbon 1s spectrum (Figure 2C), the characteristic peak of BOC/BOI-0.5 at 284.8 eV corresponds to C-C bonds, and the other characteristic peak (289.1 eV) is from C-O=C (Gao et al., 2021). Compared with BOC, the C 1s peak of BOC/BOI-0.5 is shifted to a lower energy, perhaps due to partial conversion of BOC to BOI. The X-ray spectrum of iodine's 3d is shown in Figure 2D. The binding energies of BOC/BOI-0.5 are about 619.2 eV (I $3d_{5/2}$) and 630.7 eV (I $3d_{3/2}$), indicating that the valence state of iodine is -1 (Cao et al., 2012). And the high energy shift of the I 3d doublet peaks of BOC/BOI-0.5 compared to BiOI (630.5 and 619.0 eV) can also be observed. This is because some of the CO_3^{2-} ions of the BOC component in BOC/BOI-0.5 have been replaced by I^- ions to form BOI, resulting in a corresponding increase in the binding energy of I^- in BOC/BOI-0.5 (Zhou et al., 2020). These data verify the existence of both BOC and BOI in BOC/BOI-0.5, and that the binding energy of Bi, O, C and I has shifted compared with BOC and BOI, which confirms the formation of heterojunctions in BOC/BOI-0.5.

Supplementary Figure S2 presents scanned electron micrographs of BOC, BOI and BOC/BOI-X. All show a 2D-nanosheet structure. Transmission electron micrographs further confirm that BOC/BOI-0.5 is a 2D nanosheet composed of a large number of nanosheets of different sizes (Figures 3C,D). The nanosheets are very thin compared with BOC (Figure 3A) and

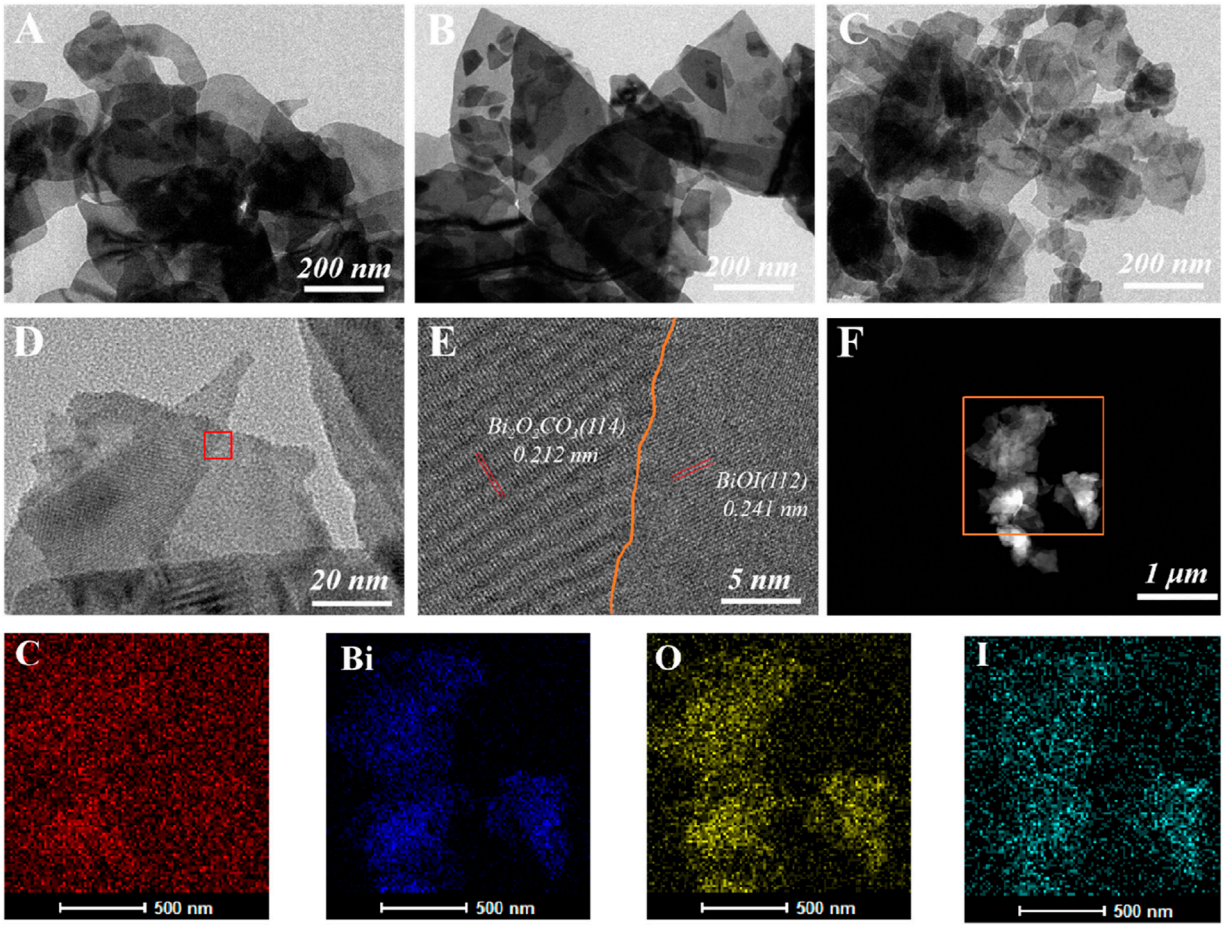

FIGURE 3
TEM images of **(A)** BOC, **(B)** BOI and **(C)** BOC/BOI-0.5; **(D,E)** high resolution transmission electron micrographs of BOC/BOI-0.5, and **(F)** STEM and element mapping image.

BOI (Figure 3B), and most of them are translucent under the electron beam, which is consistent with SEM observations. The lattice spacings measured in Figure 3E are 0.212 nm and 0.241 nm, corresponding to the (114) crystal plane of BOC (Feng et al., 2021) and the (112) crystal plane of BOI (Yang et al., 2021), respectively. By analyzing the STEM images (Figure 3F) and the corresponding EDX element mapping of BOC/BOI, the distribution of Bi, O, I and C appears uniform, indicating that BOC and BOI grow effectively coupled, resulting in interfacial interaction and forming 2D/2D heterostructures.

Nitrogen adsorption-desorption experiments were used to study the effect of specific surface area on photocatalytic performance. As shown in Figure 4A, all of the samples tested had type IV absorption curves (Hou et al., 2020a). The specific surface area of the BOC was 13.83 $m^2 g^{-1}$; that of the BOI was 10.08 $m^2 g^{-1}$ and for the BOC/BOI-0.5 material it was 15.63 $m^2 g^{-1}$. The slightly greater specific surface area of the BOC/BOI-0.5 compared to pure BOC and BOI may be due to the coupled growth of BOC and BOI (Liang et al., 2019). In addition, SEM images in Supplementary Figure S2 showed that pure BOC and BOI nanosheets have serious stacking and agglomeration. On the contrary, BOC/BOI-0.5 nanosheets showed oblique angles, resulting in more pore structures. But the data show that the specific surface area of the catalyst did not change significantly, indicating that the specific surface area had no significant effect on the photocatalytic performance. Figure 4B shows the pore size profile. All are in the range from 2 to 120 nm.

The transient photocurrent responses of BOC, BOI and BOC/BOI-0.5 are shown in Figure 4C (Jin et al., 2019). The photocurrent densities of the BOC and BOI electrodes were 0.02 μA cm^{-2} and 0.04 μA cm^{-2}, while the photocurrent density of BOC/BOI-0.5 ranged up to 0.40 μA cm^{-2}, as much as 20 times greater. The BOC/BOI-0.5 electrode's high photocurrent density was due to the formation of 2D/2D heterostructures and the high mobility photoinduced e^--h^+ pairs (Tian et al., 2019). Under the same conditions, the

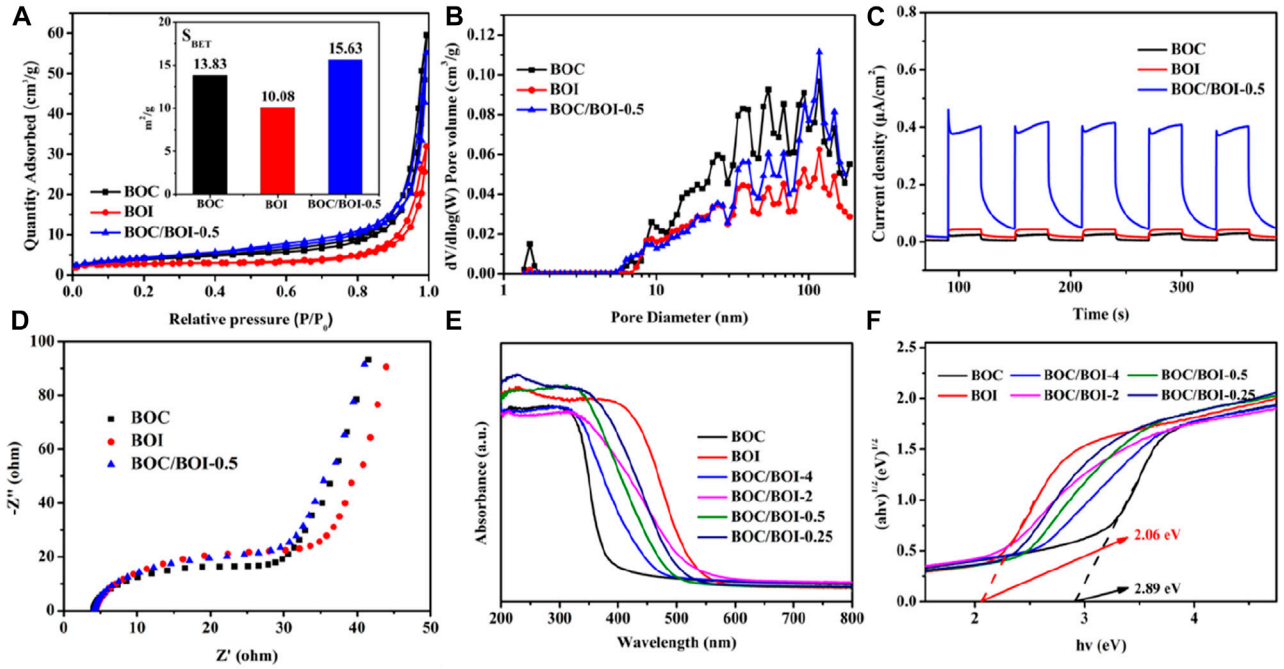

FIGURE 4
(A) Nitrogen adsorption isotherms and BET areas; **(B)** pore size distributions; **(C)** photocurrent; **(D)** Electrochemical impedence spectra of BOC, BOI and BOC/BOI-0.5; **(E,F)** UV-visible diffuse reflectance spectra.

enhanced effects of BOC/BOI heterojunctions on interface charge transfer are reflected in the EIS data. As Figure 4D shows, BOC/BOI-0.5 has a smaller Nyquist radius and interface charge transfer resistance in the dark than either BOC or BOI. So coupling BOC with BOI is an effective way to improve the photoinduced e^{-}-h^{+} pair separation and interfacial charge transfer (Yu et al., 2018).

The UV-visible diffuse reflectance spectra (Figures 4E, F) further emphasize the fine performance of the BOC/BOI photocatalysts. In Figure 4E, BOC absorbs visible light only weakly, while BOI absorbs almost all of it. The BOC/BOI composites exhibit a blend of the absorption characteristics of BOC and BOI. Since BOC and BOI form a heterojunctions (Li et al., 2023), the strong electric field generated within can accelerate charge transport and facilitate light energy conversion (Jin et al., 2021). The bandgap energy of a semiconductor can be calculated as $\alpha hv = A\,(hv\text{-}E_g)^{n/2}$ where α is the absorption coefficient, h is Planck's constant (eV), v is the optical frequency (Hz), E_g is the band gap (eV), and A is a fitting a constant. n depends on the optical conversion of the semiconductor (n = 1 for direct conversion, n = 4 for indirect conversion) (Liu et al., 2021a). $Bi_2O_2CO_3$ and BiOI are indirect bandgap semiconductors (n = 4) (Song et al., 2015; Feng et al., 2021). From the plot of $(\alpha hv)^{1/2}$ *versus* (hv) in Figure 4F, the E_g of BOC is 2.06 eV and that of BOI is 2.89 eV.

The photoelectrochemical properties of the photocatalyst under visible light irradiation were studied in terms of photocatalytic degradation of RhB. Figure 5A shows that the dark adsorption efficiency of BOC/BOI-0.5 was greatly improved compared with BOC or BOI, and the removal of RhB after 2 h was also significantly increased (Wang et al., 2023). The detailed explanation is presented in Section 3.2. It is worth noting, though, that the dark adsorption and photocatalytic effect of BOC/BOI-4 is even worse than that of BOI. However, as the amount of KI increases, the proportion of BOI in the BOC/BOI composite increases, and the dark adsorption and photocatalytic effect gradually increase, reaching an optimum with the best effect at BOC/BOI-0.5. With more KI the photocatalytic performance begins to decrease. In Supplementary Table S1 a linear fit of different BOC/BOI composites for RhB photocatalytic degradation (Figure 5B) suggested that the oxidation reaction kinetics are quasi-first-order ($\ln (C_0/C) = kt$, $R^2 > 0.99$) (Meng et al., 2019). The k value thus estimated for BOC is 0.0025 min^{-1}, that for BOI is 0.0096min^{-1} and for BOC/BOI-0.5 the calculation gives 0.024 min^{-1}. BOC/BOI-0.5's photocatalytic degradation rate is almost 10 times that of BOC and 2.5 times that of BOI.

BOC/BOI-0.5's dark adsorption and photocatalytic degradation were also tested with bisphenol A (BPA), Ciprofloxacin (CIP) and Tetracycline (TC) (Cai et al., 2023). Figure 5C shows that more than 50% of the any of them in 2 h. Tetracycline degradation reached about 90% in 40 min. So BOC/BOI-0.5 is also suitable for treating other organic pollutants. In Figure 5D, EDTA-2Na, benzoic acid and isopropyl alcohol were added to quench h^{+}, $\bullet O_2^{-}$ and •OH, respectively, the main reactive radicals in the photocatalytic process. The quenching

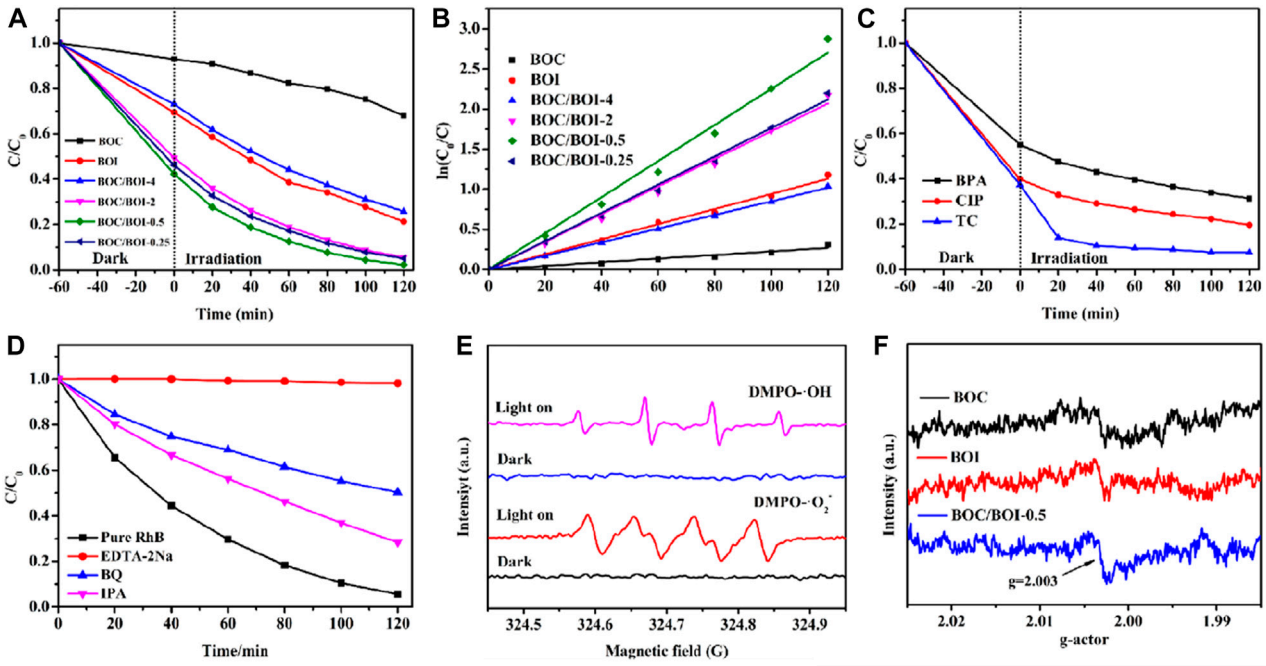

FIGURE 5
(A) Dark adsorption efficiency and photocatalytic degradation of RhB; **(B)** the pseudo-first-order kinetics of each sample; **(C)** dark adsorption and photocatalytic degradation efficiency of other pollutants, **(D)** experimental results of active group capture, **(E)** EPR with ·OH and $\cdot O_2^-$ as the active group and **(F)** EPR oxygen hole analysis.

greatly inhibited the degradation of RhB was inhibited, so h^+, $\bullet O_2^-$ and •OH are involved in the photocatalytic process. Among them, h^+ plays a leading role, probably because photogenerated electrons and holes react with O_2 and H_2O to produce $\bullet O_2^-$ and •OH, which then remove pollutants (Liu et al., 2020). EPR tests for active groups (Figure 5E) further confirmed the main active substances in the degradation process. In addition, oxygen holes (Figure 5F) were detected using EPR. Using DMPO spin adducts to capture $\bullet O_2^-$ and •OH radicals, no signal was found under dark conditions, but •OH and $\bullet O_2^-$ radical signal peaks were observed under light irradiation (Liu et al., 2021a). In the EPR oxygen vacancy analysis (Figure 5F), a peak of BOC/BOI-0.5 at g = 2.003 was observed, which proves that there are significant oxygen vacancies in BOC/BOI-0.5 (Zhao et al., 2019b). These results are consistent with those of the quenching experiments, further demonstrating the active groups that play a major role in the photocatalytic process (Geng et al., 2022).

3.2 Mechanism

Taken together, these results suggest a possible reaction mechanism. The band edge positions of BOC and BOI can be calculated as $E_{CB} = X - E_e - 0.5E_g$, and $E_{VB} = E_{CB} + E_g$ (Song et al., 2015), X here is the electronegativity of the semiconductor, E_e is about 4.5 eV, and E_g is the bandgap energy (Figure 4F). Using the formulas, the VB of BOC can be calculated as 3.59 eV and its CB as 0.70 eV. For BiOI the values are 2.74 eV and 0.68 eV, and for BOI they are 2.85 eV and 0.79 eV. A schematic diagram of the band structures of BOC and BOI is shown in Figure 6. When irradiated, e^- and h^+ will be generated, and they will interact with oxygen molecules to produce superoxide radical ($\bullet O_2$-). Photoinduced h^+ interacts with water to produce •OH, which is finally decomposed by the interaction between the two radicals and pollutants (Hou et al., 2021b).

Taken together, these findings suggest that the photocatalytic mechanism as below:

i. The nested band structure of $Bi_2O_2CO_3$ and BiOI seems to be unfavorable for photogenerated carrier separation (Feng et al., 2021). However, BOC and BOI are n-type and p-type semiconductors, respectively, and p-n heterojunction systems can generate a strong electric field at the contact interface due to the large difference in Fermi levels. In an electric field, $\bullet O_2$- and •OH will move in opposite directions, which will facilitate separation. Because the Fermi levels of BOC and BOI are very different, after they form a p-n heterojunction the energy band of p-type BOI shifts up along its Fermi level. However, the energy band of n-type

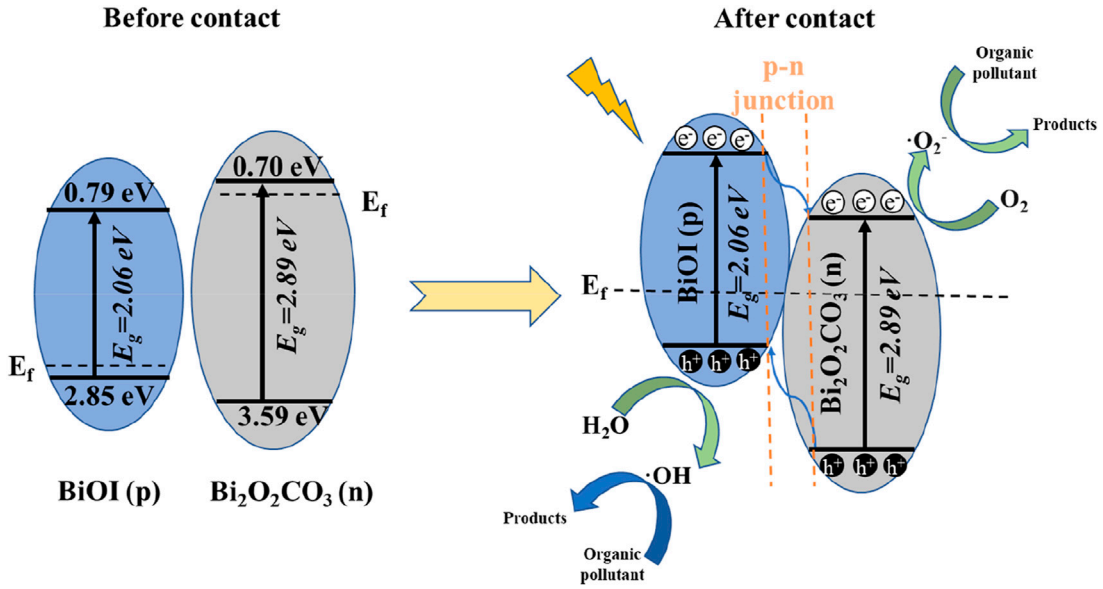

FIGURE 6
Schematic diagram of the photocatalytic reaction mechanism of $Bi_2O_2CO_3$/BiOI under visible light irradiation.

BOC moves downward along its Fermi level, which balances the Fermi levels of the BOC and BOI (Lu et al., 2021).

ii. The CB edge potential of BOI is more negative than that of BOC, so the light-induced electrons on the BOI surface easily migrate to the CB of BOC, while the holes are transferred in the opposite direction. The efficiency of separation of the photoinduced carriers is thus greatly improved, which gives the BOC/BOI composite a better ability to degrade pollutants.

iii. Oxygen vacancy (OV) is a kind of metal oxide defects. In this work, it is the separation of oxygen in the lattice caused by metal oxides at high temperature, which leads to oxygen loss and the formation of OVs. The existence of OVs makes the Fermi energy level of oxide move upward, and defect energy level appears in the band gap, thus reducing the band width and improving the light absorption performance. In addition, OVs promote the conversion of excitons into carriers, and accelerate the reduction reaction on the catalyst surface, leading to the separation of carriers. Moreover, the OVs may optimize the adsorption energy of reactants on the catalyst surface, thereby reducing the reaction energy barrier and promoting molecular activation. Thus, OVs plays a synergistic role with nearby active metal sites on the catalyst surface, and photo-generated charge carriers (e^--h^+) can then be effectively separated.

iv. At the same time, e^- can participate in the degradation of pollutants by reacting with dissolved oxygen to produce oxidizing $\cdot O_2^-$ free radicals. The h^+ react with H_2O (or OH) to produce strongly oxidizing •OH to oxidize organic pollutants. As one of the active substances, h^+ can also directly oxidize pollutants.

v. RhB can be degraded under the combined action of h^+, $\cdot O_2^-$ and •OH.

vi. In the process of RhB degradation, possible sensitization pathways should be considered. RhB may also be excited and inject electrons and residual holes from the excited state RhB* into the heterostructure. The residual holes will then further participate in the degradation reaction (Song et al., 2015). Therefore, the obtained BOC/BOI-0.5 with 2D/2D heterojunction structure is endowed with synergistic effects, which can superior to some other heterojunction materials (as shown in Supplementary Table S2)

4 Conclusion

Heterostructured BOC/BOI photocatalytic materials with tunable content have been prepared successfully. The BOC/BOI composite photocatalyst showed greater photocatalytic activity in the degradation of pollutants such as RhB than pure BOC or BOI. The composite's photodegradation rate of RhB was 9.6 times that of pure BOC. The enhanced photocatalytic activity of BOC/BOI-0.5 largely depends on the p-n heterojunction structure of BOC and BOI. BOC/BOI-0.5 has good interfacial contact and oxygen vacancies. SEM and TEM images confirm that BOC/BOI-0.5 has an ultra-thin nanosheet structure. Photoinduced holes are the main

active elements in BOC/BOI-0.5 for the photocatalytic degradation of organic compounds. And BOC/BOI-0.5 also degrades other organic pollutants. It is hoped that in the future this method will be widely applied to the synthesis of other visible light-driven photocatalysts containing bismuth heterostructures with controllable structure.

Data availability statement

The original contributions presented in the study are included in the article/Supplementary Materials, further inquiries can be directed to the corresponding authors.

Author contributions

XW and WP: conceptualization, data curation, formal analysis, investigation, methodology, writing—original draft and editing. NQ, LY, and RJ: methodology, experiment, formal analysis, writing–review and editing. DW and ZH: Writing–review and editing. JH: writing—original draft, visualization, methodology, formal analysis, writing—review and editing.

Funding

This work was carried out by the financial support from the National Natural Science Foundation of China (No. 52100014), Natural Science Foundation of Shandong Province (No. ZR2019MEM025), Open Project Fund of Anhui Key Laboratory of Mine Water Resources Utilization (Suzhou University) (No. KMWRU202102), Yangzhou University High-end Talent Support Program and the "Qinglan Project" of Jiangsu Universities.

Conflict of interest

Authors DW and ZH were employed by Jiangxi Xinda Hangke New Materials Technology Co., Ltd.

The remaining authors declare that the research was conducted in the absence of any commercial or financial relationships that could be construed as a potential conflict of interest.

Publisher's note

All claims expressed in this article are solely those of the authors and do not necessarily represent those of their affiliated organizations, or those of the publisher, the editors and the reviewers. Any product that may be evaluated in this article, or claim that may be made by its manufacturer, is not guaranteed or endorsed by the publisher.

Supplementary material

The Supplementary Material for this article can be found online at: https://www.frontiersin.org/articles/10.3389/fchem.2022.1102528/full#supplementary-material

References

Cai, M., Liu, Y., Wang, C., Lin, W., and Li, S. (2023). Novel $Cd_{0.5}Zn_{0.5}S/Bi_2MoO_6$ S-scheme heterojunction for boosting the photodegradation of antibiotic enrofloxacin: Degradation pathway, mechanism and toxicity assessment. *Sep. Purif. Technol.* 304, 122401. doi:10.1016/j.seppur.2022.122401

Cao, J., Li, X., Lin, H., Chen, S., and Fu, X. (2012). *In situ* preparation of novel p-n junction photocatalyst $BiOI/(BiO)_2CO_3$ with enhanced visible light photocatalytic activity. *J. Hazard. Mater.* 239–240, 316–324. doi:10.1016/j.jhazmat.2012.08.078

Chen, C., Jiang, T., Hou, J., Zhang, T., Zhang, G., Zhang, Y., et al. (2022). Oxygen vacancies induced narrow band gap of BiOCl for efficient visible-light catalytic performance from double radicals. *J. Mater. Sci. Technol.* 114, 240–248. doi:10.1016/j.jmst.2021.12.006

Chen, Y., Zhou, Y., Dong, Q., and Ding, H. (2018). One-step *in situ* synthesis of $BiOCl/(BiO)_2CO_3$ composite photocatalysts with exposed high-energy {001} facets. *CrystEngComm* 20 (48), 7838–7850. doi:10.1039/c8ce01608a

Di, J., Xia, J., Li, H., Guo, S., and Dai, S. (2017). Bismuth oxyhalide layered materials for energy and environmental applications. *Nano Energy* 41, 172–192. doi:10.1016/j.nanoen.2017.09.008

Ding, P., Di, J., Chen, X., Zhao, J., Gu, K., Zhang, Y., et al. (2019). Partially etched $Bi_2O_2CO_3$ by metal chloride for enhanced reactive oxygen species generation: A tale of two strategies. *Appl. Catal. B Environ.* 245, 325–333. doi:10.1016/j.apcatb.2018.12.047

Feng, R., Lei, W., Liu, G., and Liu, M. (2018). Visible- and NIR-light responsive black-phosphorus-based nanostructures in solar fuel production and environmental remediation. *Adv. Mat.* 30 (49), e1804770. doi:10.1002/adma.201804770

Feng, Y., Zhang, Z., Zhao, K., Lin, S., Li, H., and Gao, X. (2021). Photocatalytic nitrogen fixation: Oxygen vacancy modified novel micro-nanosheet structure $Bi_2O_2CO_3$ with band gap engineering. *J. Colloid Interface Sci.* 583, 499–509. doi:10.1016/j.jcis.2020.09.089

Gao, B., Sun, M., Ding, W., Ding, Z., and Liu, W. (2021). Decoration of γ-graphyne on TiO_2 nanotube arrays: Improved photoelectrochemical and photoelectrocatalytic properties. *Appl. Catal. B Environ.* 281, 119492. doi:10.1016/j.apcatb.2020.119492

Geng, J., Zhao, L., Wang, M., Dong, G., and Ho, W. (2022). The photocatalytic NO-removal activity of g-C_3N_4 significantly enhanced by the synergistic effect of Pd^0 nanoparticles and N vacancies. *Environ. Sci. Nano* 9 (2), 742–750. doi:10.1039/d1en00937k

Hamza, M. A., El-Shazly, A. N., Tolba, S. A., and Allam, N. K. (2020). Novel Bi-based photocatalysts with unprecedented visible light-driven hydrogen production rate: Experimental and DFT insights. *Chem. Eng. J.* 384, 123351. doi:10.1016/j.cej.2019.123351

Hou, J., Jiang, T., Wang, X., Zhang, G., Zou, J., and Cao, C. (2021a). Variable dimensional structure and interface design of g-C_3N_4/BiOI composites with oxygen vacancy for improving visible-light photocatalytic properties. *J. Clean. Prod.* 287, 125072. doi:10.1016/j.jclepro.2020.125072

Hou, J., Tu, X., Wu, X., Shen, M., Wang, X., Wang, C., et al. (2020a). Remarkable cycling durability of lithium-sulfur batteries with interconnected mesoporous hollow carbon nanospheres as high sulfur content host. *Chem. Eng. J.* 401, 126141. doi:10.1016/j.cej.2020.126141

Hou, J., Zhang, T., Jiang, T., Wu, X., Zhang, Y., Tahir, M., et al. (2021b). Fast preparation of oxygen vacancy-rich 2D/2D bismuth oxyhalides-reduced graphene oxide composite with improved visible-light photocatalytic properties by solvent-free grinding. *J. Clean. Prod.* 328, 129651. doi:10.1016/j.jclepro.2021.129651

Hou, W., Xu, H., Cai, Y., Zou, Z., Li, D., and Xia, D. (2020b). Precisely control interface OVs concentration for enhance 0D/2D $Bi_2O_2CO_3$/BiOCl photocatalytic performance. *Appl. Surf. Sci.* 530, 147218. doi:10.1016/j.apsusc.2020.147218

Jin, X., Lv, C., Zhou, X., Xie, H., Sun, S., Liu, Y., et al. (2019). A bismuth rich hollow $Bi_4O_5Br_2$ photocatalyst enables dramatic CO_2 reduction activity. *Nano Energy* 64, 103955. doi:10.1016/j.nanoen.2019.103955

Jin, X., Xu, Y., Zhou, X., Lv, C., Huang, Q., Chen, G., et al. (2021). Single-atom Fe triggers superb CO_2 ohotoreduction on a bismuth-rich catalyst. *ACS Mater. Lett.* 3 (4), 364–371. doi:10.1021/acsmaterialslett.1c00091

Li, M., Huang, H., Yu, S., Tian, N., and Zhang, Y. (2018). Facet, junction and electric field engineering of bismuth-based materials for photocatalysis. *ChemCatChem* 10 (20), 4477–4496. doi:10.1002/cctc.201800859

Li, S., Cai, M., Liu, Y., Wang, C., Lv, K., and Chen, X. (2022a). S-scheme photocatalyst TaON/Bi_2WO_6 nanofibers with oxygen vacancies for efficient abatement of antibiotics and Cr(VI): Intermediate eco-toxicity analysis and mechanistic insights. *Chin. J. Catal.* 43, 2652–2664. doi:10.1016/S1872-2067(22)64106-8

Li, S., Cai, M., Liu, Y., Wang, C., Yan, R., and Chen, X. (2023). Constructing $Cd_{0.5}Zn_{0.5}S$/Bi_2WO_6 S-scheme heterojunction for boosted photocatalytic antibiotic oxidation and Cr(VI) reduction. *Adv. Powder Mater.* 2, 100073. doi:10.1016/J.APMATE.2022.100073

Li, S., Cai, M., Wang, C., Liu, Y., Li, N., Zhang, P., et al. (2022b). Rationally designed Ta_3N_5/BiOCl S-scheme heterojunction with oxygen vacancies for elimination of tetracycline antibiotic and Cr(VI): Performance, toxicity evaluation and mechanism insight. *J. Mater. Sci. Technol.* 123, 177–190. doi:10.1016/j.jmst.2022.02.012

Li, Y., Jiang, Z., Dong, G., and Ho, W. (2022c). Construction and activity of an all-organic heterojunction photocatalyst based on melem and pyromellitic dianhydride. *ChemSusChem* 15 (12), e202200477. doi:10.1002/cssc.202200477

Liang, C., Niu, C. G., Zhang, L., Wen, X. J., Yang, S. F., Guo, H., et al. (2019). Construction of 2D heterojunction system with enhanced photocatalytic performance: Plasmonic Bi and reduced graphene oxide co-modified Bi_5O_7I with high-speed charge transfer channels. *J. Hazard. Mater.* 361, 245–258. doi:10.1016/j.jhazmat.2018.08.099

Liu, D., Chen, D., Li, N., Xu, Q., Li, H., He, J., et al. (2020). Surface engineering of g-C3 N4 by stacked BiOBr sheets rich in oxygen vacancies for boosting photocatalytic performance. *Angew. Chem. Int. Ed.* 59 (11), 4519–4524. doi:10.1002/anie.201914949

Liu, J., Dong, G., Jing, J., Zhang, S., Huang, Y., and Ho, W. (2021a). Photocatalytic reactive oxygen species generation activity of TiO_2 improved by the modification of persistent free radicals. *Environ. Sci. Nano* 8 (12), 3846–3854. doi:10.1039/d1en00832c

Liu, L., Hu, T., Dai, K., Zhang, J., and Liang, C. (2021b). A novel step-scheme $BiVO_4$/Ag_3VO_4 photocatalyst for enhanced photocatalytic degradation activity under visible light irradiation. *Chin. J. Catal.* 42 (1), 46–55. doi:10.1016/s1872-2067(20)63560-4

Liu, Z., Zhang, J., and Yan, W. (2018). Enhanced photoelectrochemical water splitting of photoelectrode simultaneous decorated with cocatalysts based on spatial charge separation and transfer. *ACS Sustain. Chem. Eng.* 6 (3), 3565–3574. doi:10.1021/acssuschemeng.7b03894

Lu, X., Li, Q., Wang, L., Jiang, W., Luo, R., Zhang, M., et al. (2021). Fabrication of one dimensional hierarchical WO_3/BiOI heterojunctions with enhanced visible light activity for degradation of pollutants. *RSC Adv.* 11 (27), 16608–16618. doi:10.1039/d1ra01665b

Meng, Q., Lv, C., Sun, J., Hong, W., Xing, W., Qiang, L., et al. (2019). High-efficiency Fe-mediated Bi_2MoO_6 nitrogen-fixing photocatalyst: Reduced surface work function and ameliorated surface reaction. *Appl. Catal. B Environ.* 256, 117781. doi:10.1016/j.apcatb.2019.117781

Qi, K., Jing, J., Dong, G., Li, P., and Huang, Y. (2022). The excellent photocatalytic NO removal performance relates to the synergistic effect between the prepositive NaOH solution and the g-C_3N_4 photocatalysis. *Environ. Res.* 212, 113405. doi:10.1016/j.envres.2022.113405

Qiang, Z., Liu, X., Li, F., Li, T., Zhang, M., Singh, H., et al. (2021). Iodine doped Z-scheme $Bi_2O_2CO_3$/Bi_2WO_6 photocatalysts: Facile synthesis, efficient visible light photocatalysis, and photocatalytic mechanism. *Chem. Eng. J.* 403, 126327. doi:10.1016/j.cej.2020.126327

Sakthivel, T., Huang, X., Wu, Y., and Rtimi, S. (2020). Recent progress in black phosphorus nanostructures as environmental photocatalysts. *Chem. Eng. J.* 379, 122297. doi:10.1016/j.cej.2019.122297

Shi, Y., Xiong, X., Ding, S., Liu, X., Jiang, Q., and Hu, J. (2018). *In-situ* topotactic synthesis and photocatalytic activity of plate-like BiOCl/2D networks Bi_2S_3 heterostructures. *Appl. Catal. B Environ.* 220, 570–580. doi:10.1016/j.apcatb.2017.08.074

Song, P., Xu, M., and Zhang, W. (2015). Sodium citrate-assisted anion exchange strategy for construction of $Bi_2O_2CO_3$/BiOI photocatalysts. *Mater. Res. Bull.* 62, 88–95. doi:10.1016/j.materresbull.2014.11.002

Tang, X., Huang, Z., Cao, Y., Zhang, R., Dong, F., and Zhou, Y. (2020). Mo promotes interfacial interaction and induces oxygen vacancies in 2D/2D of Mo-g-C_3N_4 and $Bi_2O_2CO_3$ photocatalyst for enhanced NO oxidation. *Ind. Eng. Chem. Res.* 59 (20), 9509–9518. doi:10.1021/acs.iecr.0c00777

Tian, L., Min, S., and Wang, F. (2019). Integrating noble-metal-free metallic vanadium carbide cocatalyst with CdS for efficient visible-light-driven photocatalytic H_2 evolution. *Appl. Catal. B Environ.* 259, 118029. doi:10.1016/j.apcatb.2019.118029

Wang, C., Yan, R., Cai, M., Liu, Y., and Li, S. (2023). A novel organic/inorganic S-scheme heterostructure of TCPP/$Bi_{12}O_{17}Cl_2$ for boosting photodegradation of tetracycline hydrochloride: Kinetic, degradation mechanism, and toxic assessment. *Appl. Surf. Sci.* 610, 155346. doi:10.1016/j.apsusc.2022.155346

Wang, H., Liang, Y., Liu, L., Hu, J., Wu, P., and Cui, W. (2017). Enriched photoelectrocatalytic degradation and photoelectric performance of BiOI photoelectrode by coupling rGO. *Appl. Catal. B Environ.* 208, 22–34. doi:10.1016/j.apcatb.2017.02.055

Xu, B., An, Y., Liu, Y., Qin, X., Zhang, X., Dai, Y., et al. (2017). Enhancing the photocatalytic activity of BiOX (X = Cl, Br, and I), $(BiO)_2CO_3$ and Bi_2O_3 by modifying their surfaces with polar organic anions, 4-substituted thiophenolates. *J. Mat. Chem. A* 5 (27), 14406–14414. doi:10.1039/c7ta03970k

Xu, M., Yang, J., Sun, C., Liu, L., Cui, Y., and Liang, B. (2020). Performance enhancement strategies of Bi-based photocatalysts: A review on recent progress. *Chem. Eng. J.* 389, 124402. doi:10.1016/j.cej.2020.124402

Yang, J., Su, H., Wu, Y., Li, D., Zhang, D., Sun, H., et al. (2021). Facile synthesis of kermesinus BiOI with oxygen vacancy for efficient hydrogen generation. *Chem. Eng. J.* 420, 127607. doi:10.1016/j.cej.2020.127607

Yu, S., Zhang, Y., Dong, F., Li, M., Zhang, T., and Huang, H. (2018). Readily achieving concentration-tunable oxygen vacancies in $Bi_2O_2CO_3$: Triple-functional role for efficient visible-light photocatalytic redox performance. *Appl. Catal. B Environ.* 226, 441–450. doi:10.1016/j.apcatb.2017.12.074

Zhang, L., Yang, J., Zhao, X., Xiao, X., Sun, F., Zuo, X., et al. (2020). Small-molecule surface-modified bismuth-based semiconductors as a new class of visible-light-driven photocatalytic materials: Structure-dependent photocatalytic properties and photosensitization mechanism. *Chem. Eng. J.* 380, 122546. doi:10.1016/j.cej.2019.122546

Zhao, W., Feng, Y., Huang, H., Zhou, P., Li, J., Zhang, L., et al. (2019a). A novel Z-scheme Ag_3VO_4/$BiVO_4$ heterojunction photocatalyst: Study on the excellent photocatalytic performance and photocatalytic mechanism. *Appl. Catal. B Environ.* 245, 448–458. doi:10.1016/j.apcatb.2019.01.001

Zhao, Z., Cao, Y., Dong, F., Wu, F., Li, B., Zhang, Q., et al. (2019b). The activation of oxygen through oxygen vacancies in BiOCl/PPy to inhibit toxic intermediates and enhance the activity of photocatalytic nitric oxide removal. *Nanoscale* 11 (13), 6360–6367. doi:10.1039/c8nr10356a

Zhou, T., Zhang, H., Zhang, X., Yang, W., Cao, Y., and Yang, P. (2020). BiOI/$Bi_2O_2CO_3$ Two-dimensional heteronanostructures with boosting charge carrier separation behavior and enhanced visible-light photocatalytic performance. *J. Phys. Chem. C* 124 (37), 20294–20308. doi:10.1021/acs.jpcc.0c06833

Zu, X., Zhao, Y., Li, X., Chen, R., Shao, W., Wang, Z., et al. (2021). Ultrastable and efficient visible-light-driven CO_2 reduction triggered by regenerative oxygen-vacancies in $Bi_2O_2CO_3$ nanosheets. *Angew. Chem. Int. Ed.* 60 (25), 13840–13846. doi:10.1002/anie.202101894